

Unveiling gas phase H₂NCO radical: Laboratory rotational spectroscopy and interstellar search toward IRAS 16293-2422

Marie-Aline Martin-Drumel¹, Audrey Coutens², Jean-Christophe Loison³, Jes K. Jørgensen⁴, and Olivier Pirali¹

¹ Université Paris-Saclay, CNRS, Institut des Sciences Moléculaires d'Orsay, 91405 Orsay, France
e-mail: marie-aline.martin@universite-paris-saclay.fr

² Institut de Recherche en Astrophysique et Planétologie, Université de Toulouse, UT3-PS, CNRS, CNES, 9 av. du Colonel Roche, 31028 Toulouse Cedex 4, France

³ Université Bordeaux, CNRS, Institut des Sciences Moléculaires, 33400 Talence, France

⁴ Niels Bohr Institute, University of Copenhagen, Øster Voldgade 5–7, DK-1350 Copenhagen K., Denmark

Received ...; accepted ...

ABSTRACT

Context. The carbamoyl radical (H₂NCO) is believed to play a central role in the ice-grain chemistry of crucial interstellar complex organic molecules as formamide and acetamide. Yet, little is known about this radical that remains elusive in laboratory gas-phase experiments.

Aims. In order to enable interstellar searches of H₂NCO, we have undertaken a mandatory laboratory characterisation of its pure rotational spectrum.

Methods. We report the gas-phase laboratory detection of H₂NCO, produced by H-atom abstraction from formamide, using pure rotational spectroscopy at millimetre and submillimetre wavelengths. Millimetre-wave data were acquired using chirped-pulse Fourier-transform spectroscopy while submillimetre-wave ones were obtained using Zeeman-modulated spectroscopy. Experimental measurements were guided by quantum-chemical calculations at the ω B97X-D/cc-pVQZ level of theory. Interstellar searches for the radical have been undertaken on the Protostellar Interferometric Line Survey (PILS) towards the solar-type protostar IRAS 16293–2422.

Results. From the assignment and fit of experimental transitions up to 660 GHz, reliable spectroscopic parameters for H₂NCO in its ground vibrational state have been derived, enabling accurate spectral predictions. No transitions of the radical were detected on the PILS survey. The inferred upper limit shows that H₂NCO abundance is at least 60 times below that of formamide and 160 times below that of HNCO in this source; a value that is in agreement with predictions from a physico-chemical model of this young protostar.

Key words. methods: laboratory: molecular – techniques: spectroscopic – astrochemistry – ISM: abundances – submillimeter: general

1. Introduction

Alongside isocyanic acid (HNCO) and formamide (H₂NCHO), the carbamoyl radical (H₂NCO, also known such as NH₂CO and carbamyl in the literature) is one of the simplest molecules that incorporates the four most abundant atomic elements vital for biological systems, namely, C, H, O, and N. Because it possesses the peptide bond (NH–C(=O)–), it holds significant potential as a key molecular precursor under prebiotic and abiotic conditions (e.g., Poskrebyshev 2017). H₂NCO is found, both experimentally and theoretically, to be of key importance in the ice-grain chemical networks of interstellar complex organic molecules (iCOMs; e.g., Haupa et al. 2019). Its formation under interstellar conditions is best explained by reactions occurring on grains, namely H-atom abstraction from formamide (e.g., Förstel et al. 2016; Haupa et al. 2019), H-addition to HNCO (e.g., Miller & Melius 1992; Song & Kästner 2016), or to a lower extent by the reaction between NH₂ and CO (e.g., Agarwal et al. 1985; Bredehöft et al. 2017; Ligterink et al. 2018b). These sequences are incorporated into current chemical models of gas-grain chemistry (Garrod et al. 2022; Belloche et al. 2019). Once formed, the H₂NCO radical is believed to be a central intermediate in the formation of many interstellar molecules, from formamide (Raunier et al. 2004; Haupa et al. 2019) and HNCO (Hubbard et al. 1975) to larger amides and many iCOMs such as urea

(NH₂C(O)NH₂, Agarwal et al. 1985; Ligterink et al. 2018b; Raunier et al. 2004; Slate et al. 2020), acetamide (CH₃C(O)NH₂ Ligterink et al. 2018b; Belloche et al. 2019; Garrod et al. 2022; Zeng et al. 2023), propiolamide (NH₂C(O)C₂H, Alonso et al. 2021), and acrylamide (NH₂C(O)C₂H₃, Kolesniková et al. 2022). This common chemistry also potentially explains the observed correlations of the abundances of numerous iCOMs (see, e.g., Bisschop et al. 2007; López-Sepulcre et al. 2015; Gorai et al. 2020; Ligterink et al. 2022). Additionally, besides the species aforementioned, other molecules containing the NCO bond—and that could thus be related to H₂NCO—have already been detected in the interstellar medium; namely the NCO radical (Marcelino et al. 2018a), N-protonated isocyanic acid H₂NCO⁺ (Gupta et al. 2013), methyl isocyanate CH₃NCO (Halfen et al. 2015; Cernicharo et al. 2016), and ethyl isocyanate C₂H₅NCO (Rodríguez-Almeida et al. 2021).

In contrast to the vast literature investigating H₂NCO formation and reactivity, only a few studies have reported a direct detection of the species, all of which were condensed phase investigations. In the late 1960s, the radical was observed using electron paramagnetic resonance spectroscopy. However, some ambiguity persisted regarding the observed isomer, either a σ -electron radical (hence H₂NCO, Livingston & Zeldes 1967; Yonezawa et al. 1968, 1969) or π -electron one (HNCHO, Smith

& Wood 1966; Fox & Smith 1968). The latter possibility was later deemed unlikely (Andrews 1970). More recently, matrix isolation experiments have enabled the observation of the infrared spectrum of the radical, produced by H-addition to HNCO (Pettersson et al. 1999) or H-abstraction from formamide (Haupa et al. 2019). The vibrational band assignments were supported by quantum chemical calculations (Pettersson et al. 1999). Other theoretical studies have also dived into the energetics of the [C,H₂,N,O] isomeric family (Shapley & Bacskay 1999) and the thermochemistry of H₂NCO (Shapley & Bacskay 1999; Nagy et al. 2010; Poskrebyshev 2015, 2017; Nguyen et al. 1996).

We here report the first detection of H₂NCO in gas-phase laboratory experiments. The radical was produced by H-atom abstraction from formamide and its pure rotational spectrum was recorded at millimetre and submillimetre wavelengths, as described in Sect. 2. Spectroscopic analysis of the experimental data has enabled the construction of a robust line frequency catalogue that was used to search for the radical towards the solar-type protostar IRAS 16293–2422 (Sect. 3).

2. Laboratory methods

2.1. Quantum chemical calculations

To initiate laboratory searches for transitions of H₂NCO, quantum chemical calculations have been performed on the species. Geometry optimisation followed by harmonic and anharmonic frequency analysis have been carried out at the ω B97X-D/cc-pVQZ level of theory (Chai & Head-Gordon 2008; Dunning 1989; Woon & Dunning 1993) providing a reliable set of spectroscopic parameters (dipole moments projections; rotational, quartic and sextic centrifugal distortion, spin-rotation, and hyperfine constants). Special care was taken to ensure that the calculations of vibration-rotation quantities were performed in the principal axis system, as recommended in McKean et al. (2008). Using Bayesian corrected rotational constants—following Lee & McCarthy (2020)—the spectral predictions are expected to be very close to the experimental features, as previously seen in Buchanan et al. (2021) and Martin-Drumel et al. (2023). All calculations were performed using the GAUSSIAN 16 suite of electronic structure programs (Frisch et al. 2016).

2.2. Synthesis of H₂NCO

The H₂NCO radical was produced by H-abstraction from formamide ($\geq 99.5\%$, Merck), a reaction initiated by F atoms themselves produced by a 50 W microwave discharge in F₂ (5% in He, Air Liquide). The process is similar to the one used in our previous works on CH₂OH, CH₂CN, and CH₂CHO radicals (Chitarra et al. 2020; Coudert et al. 2022; Chitarra et al. 2022; Chahbazian et al. 2024). The two reaction cells used to synthesise and probe the radical have been presented in detail in Chitarra et al. (2022): both are 50 mm diameter cells mainly made of Pyrex, each adapted to one of our two spectrometers. The cell used for millimetre-wave chirped-pulse measurements is of about 70 cm total length and equipped with one inlet for F-injection while the one used for submillimetre-wave measurements is about 2 m-long and equipped with three F-injection inlets. Using both cells, measurements were performed in a continuous flow ensured by a roots blower (EH250, Edwards) backed-up by a chemically graded pump (PFPE-E2M28, Edwards). Since a second potential primary product of the reaction of H-abstraction from formamide is the HNCHO radical, if abstraction occurs on the nitrogen atom instead of the carbon one,

initial searches for the signature of both radicals were performed using various pressure ratio of formamide and F₂:He mixture, the best signal of the H₂NCO radical was obtained using 5 μ bar of formamide for a total pressure of 11 μ bar. It is worth noting that the quoted pressure are only indicative as the pressure gauge was placed above the roots blower using a DN16 inlet, far downstream the probed reaction cell in order to preserve it from reactive products. Under these conditions, the pressure was similar with and without discharge.

2.3. Chirped-pulse millimetre-wave spectroscopy

A chirped-pulse Fourier-transform millimetre-wave (CP-FTMMW, Brightspec) instrument was used to perform measurements in the 75–110 GHz spectral region (W-band). Spectra were acquired using a segmented approach implemented in the high dynamic range mode of the Brightspec Edgar acquisition software, as previously detailed in Chitarra et al. (2022). Initial searches were performed for both H₂NCO and HNCHO radicals using 500,000 averaged FIDs (about 1 hour of acquisition) obtained using a pulse length of 0.5 μ s. All measurements were repeated under the same conditions after placing a permanent magnet below the volume of the cell where the precursors interact, allowing us to identify transitions affected by the magnetic field. Once signal of H₂NCO was found, multiple spectra were acquired under conditions found to maximise the production of this radical (5 μ bar of formamide and 6 μ bar of F₂/He, 0.25 μ s excitation pulse). Free induction decay (FID) signals were acquired over 4 μ s, starting 0.1 μ s after the end of the excitation pulse. To retrieve frequency domain spectra, the FIDs were Fourier transformed using a Kaiser-Bessel apodization function over the first 2 μ s since Fourier-transform over shorter FIDs yields a significant gain in signal-to-noise ratio—at the expense of the spectral resolution—which, under our experimental conditions, has proven useful to detect weak features in the spectra. The final spectrum was averaged in the frequency domain and corresponds to 2.9 million FIDs (again, a similar spectrum was recorded with a permanent magnet placed below the reaction cell). The resulting line frequency accuracies are estimated to be 100 kHz for strong, isolated lines and 200 kHz for weaker and/or broader ones.

2.4. Zeeman-modulated submillimetre-wave spectroscopy

The Zeeman-modulated submillimetre-wave spectrometer used in this study, which is an evolution from the double-modulation spectrometer we used previously (Chitarra et al. 2022), has been presented in detail in Chahbazian et al. (2024). A radio-frequency synthesizer (Rhode & Schwarz), whose 10 MHz reference signal is provided by a Rubidium clock (Stanford Research), feeds a frequency multiplication chain (Virginia Diode Inc.) operating nominally over the 75–900 GHz range. In this study, measurements were performed from 140 GHz to 660 GHz using a single path configuration in which the radiation is collimated by a teflon lens (100 mm focal length), transmitted through the reaction cell, and focused onto the detector using either an identical teflon lens or, above 330 GHz, an off-axis parabolic mirror (300 mm focal length). Schottky diode detectors (VDI) were used in the 140–220 GHz and 220–330 GHz spectral ranges and a mechanically-cooled Indium antimonide (InSb) bolometer (QMC) was employed above 330 GHz. Additionally, in the 140–220 GHz, the output radiation from the VDI chain was attenuated by about 30% (Elmika, WR5 VA-015E)

which was found to minimise the strong Fabry-Perot effect on the baseline without affecting the signal-to-noise ratio of the transitions. To operate under Zeeman modulation conditions, a 16.9 kHz sinusoidal signal—generated by a waveform generator followed by an audio amplifier—is circulating in a coil surrounding the reaction cell, resulting in an alternating magnetic field of about 3.5 Gauss. The signal received by the detector is then demodulated by a lock-in amplifier at the frequency of this sinusoidal signal.

The pressure conditions found to maximise the signal of the H₂NCO radical using chirped-pulse spectroscopy were found to also yield to the maximum of signal in Zeeman-modulated spectroscopy. Surveys around the regions where clusters of lines of H₂NCO were expected have been recorded. Thanks to the Zeeman-modulation settings, broad spectral windows, from 100 MHz to 10 GHz, were scanned in a straightforward fashion, without being affected by the signal of the precursor and the saturation effects it would have induced onto the lock-in amplifier in frequency-modulated or double-modulation spectroscopy, as shown already in Chahbazian et al. (2024). The spectra were acquired using frequency steps of 100 kHz below 440 GHz, and 200 kHz above that value. Below 330 GHz and above 440 GHz, each frequency point was averaged between 200 ms and 400 ms. In the 330–440 GHz where the signal-to-noise ratio on H₂NCO was the strongest (a combination of Boltzmann population, power of the source, sensitivity of the bolometer, and amplitude of the Zeeman splitting with respect to the width of the line), 50 ms averages were enough to reach an excellent signal-to-noise ratio for most lines (20 to 50). Finally, dedicated searches for weak *b*-type transitions (see section 3.1) were performed in the 330–660 GHz region using 5 s averaging time.

It is worth mentioning that the profile of many H₂NCO lines (in particular $K_a = 2$ ones) appears severely impacted by the effect of the magnetic field on the spin-rotation structure which results in some very asymmetrical profiles. This became particularly noticeable above 330 GHz where the signal-to-noise ratio is the strongest. We found that we could minimise this effect by positioning a polarising grid (Pure Wave Polarizers) right after the radiation source in order to filter out the small portion of non-vertically polarised radiation emitted. A second polarising grid, also selecting vertical polarisation, was placed in front of the bolometer but its effect was not as significant, presumably because the bolometer sensor is not very sensitive to the polarisation of the radiation. A conservative frequency uncertainty has been used for transitions exhibiting asymmetric profiles. Overall, these uncertainties range from 50 kHz (from intense, symmetric lines) to 300 kHz (for weak, broad, or asymmetric lines) over the entire covered spectral range.

3. Results and discussion

3.1. Spectroscopic considerations

The H₂NCO radical is planar and belongs to the C_s point group of symmetry. The molecular structure and geometrical parameters calculated in this study are displayed in Fig. 1. The calculated bond lengths and angles are in good agreement with those reported in the literature (Pettersson et al. 1999; Shapley & Baskay 1999), although we suspect that there was some exchange in the values pertaining to each H atom in Fig. 8 of Pettersson et al. (1999). The radical possesses dipole moment projections of 3.7 Debye along the *a*-axis of symmetry and 0.5 Debye along the *b*-one.

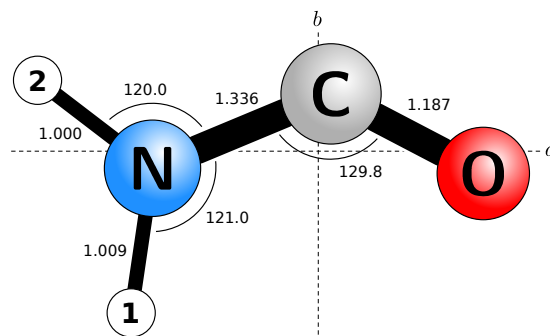


Fig. 1. Equilibrium structure of H₂NCO calculated at the ω B97X-D/cc-pVQZ level of theory. Geometrical parameters (bond lengths in angstroms and angles in degrees) and principal axes of inertia are reported. The figure was generated using the PMIFST software from the PROSPE collection of programs developed by Kisiel (2001). **1** and **2** refer to the H₁ and H₂ labelling used in the text.

H₂NCO possesses a $^2A'$ electronic ground state and nine normal modes of vibration following the irreducible representation $\Gamma = 7A' + 2A''$ (see Appendix A for vibrational frequencies and α values in the vibrationally excited states). It is a near-prolate asymmetric-top rotor with a Ray's asymmetry parameter $\kappa = -0.98$. Due to the presence of an unpaired electron ($S = 1/2$) and three atoms with non-zero nuclear spin (N, H₁ and H₂; with $I_N = 1$ and $I_{H_1} = I_{H_2} = 1/2$), each rotational energy level of N_{K_a, K_c} quantum numbers is split by electron spin-rotation coupling (into a fine structure of *J* sub-levels) and hyperfine couplings (with hyperfine levels labelled using F_1, F_2, F quantum numbers). For all non-zero nuclear spin atoms, the hyperfine structure results from coupling between the electron spin and nuclear spin. Additionally, for the ^{14}N nucleus, there is also nuclear quadrupole coupling. Because the two protons are non-equivalent, this leads to a maximum of 24 sub-levels following the coupling scheme $\mathbf{J} = \mathbf{N} + \mathbf{S}$, $\mathbf{F}_1 = \mathbf{J} + \mathbf{I}_N$, $\mathbf{F}_2 = \mathbf{F}_1 + \mathbf{I}_{H_1}$ and $\mathbf{F} = \mathbf{F}_2 + \mathbf{I}_{H_2}$.

In the present work, we observed some transitions presenting a fully resolved hyperfine structure, the effective Hamiltonian used to model the energy levels of the vibronic ground state is thus: $\mathcal{H} = \mathcal{H}_{\text{rot}} + \mathcal{H}_{\text{sr}} + \mathcal{H}_{\text{hfs,N}} + \mathcal{H}_{\text{hfs,H}_1} + \mathcal{H}_{\text{hfs,H}_2}$, where \mathcal{H}_{rot} is the Hamiltonian operator for the pure rotational energy, \mathcal{H}_{sr} that for the electron spin-rotation, $\mathcal{H}_{\text{hfs,N}}$ is the hyperfine Hamiltonian for the ^{14}N nucleus (and accounts for nuclear magnetic and nuclear quadrupole interactions), and $\mathcal{H}_{\text{hfs,H}_1}$ and $\mathcal{H}_{\text{hfs,H}_2}$ are the hyperfine structure Hamiltonians accounting for the coupling of the spins of the two protons H₁ and H₂ with the spin of the unpaired electron. The calculated spectroscopic parameters of this effective Hamiltonian are reported in Table 1.

Because H₂NCO is a light species, its pure rotational spectrum extends far into the submillimetre-wave domain, even at low temperature, as illustrated on Fig. 2. The spectral regions investigated in this study are highlighted on the figure. Due to the dipole moment projection values, *a*-type transitions dominate the spectrum; *b*-type transitions are visible in the high-frequency tail of the spectra.

3.2. Assignments and fit

We used the PGOPHER program (Western 2017) to search for, and assign, transitions of the H₂NCO radical. The final fit and spectral predictions were performed with the Pickett CALPGM suite of programs (Pickett 1991) using a Watson *S*-reduced Hamiltonian.

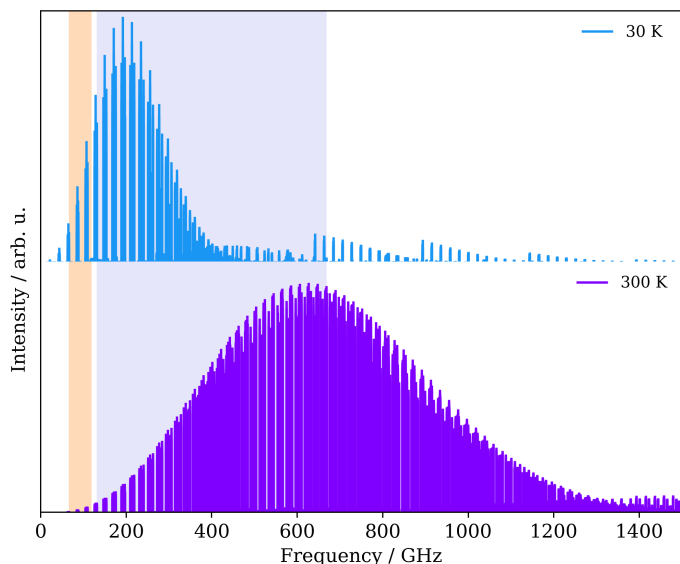


Fig. 2. Predicted pure rotational spectrum of H_2NCO (in the ground vibrational state, $\nu = 0$) up to 1.5 THz at 30 K (top) and 300 K (bottom). The spectral regions investigated in this study using the CP and Zeeman-modulated spectrometers are highlighted in orange and purple, respectively.

On the CP-FTMMW spectrum, two clusters of transitions closely matching what expected for the $N' - N'' = 4 - 3$ and $5 - 4$ transitions of H_2NCO are readily observed (Fig. 3). The detailed procedure used to retrieve a spectrum displaying only transitions from open-shell species and to identify these transitions is reported in Appendix B. Spectroscopic assignments of H_2NCO transitions were straightforward: the two clusters of lines are separated by about 21370 MHz when the calculated $B + C$ value for H_2NCO is 21425 MHz (0.3 % error) and the experimental transitions display the K_a , fine structure, and hyperfine structure patterns expected from the prediction. A closer look at the spectrum reveals that the $N' - N'' = 4 - 3$ and $5 - 4$, $K_a = 0$ lines lie only about 140 MHz and 180 MHz higher than the prediction, respectively (about 0.2 % error). In total 85 transitions (36 different frequencies) were assigned for the $N' - N'' = 4 - 3$ ($K_a = 0, 1$) and $5 - 4$ ($K_a = 0 - 3$) clusters of transitions. These initial assignments enabled preliminary adjustments of the spectroscopic constants, subsequently facilitating measurements at submillimetre wavelengths. A comparison of a portion of the CP spectrum with a simulation obtained using the final set of spectroscopic constants is shown in Appendix B.

From 146 GHz to 660 GHz, 3469 a -type transitions (1395 different frequencies) of H_2NCO have been assigned. An example of the $N' - N'' = 18 - 17$ a -type transitions, that spread over about 16 GHz, is shown in Fig. 4. Spectral acquisitions were performed mostly over small regions around the predictions. Under our experimental conditions, transitions measured using Zeeman-modulation present mostly a profile close to a second-derivative of a Gaussian line. Many of the observed transitions display a partially resolved hyperfine structure, as for example the $K_a = 3$ cluster highlighted in orange on Fig. 4. Further information about the hyperfine structure and how it was included in the fit is reported in Appendix C. Fig. 4 also illustrates the anomalously strong intensity of some K_a components compared to what expected from the simulation (for instance the $K_a = 2$, $K_a + K_c = J$ cluster around 389400 MHz) and asymmetry of some components (for instance the lowest and highest

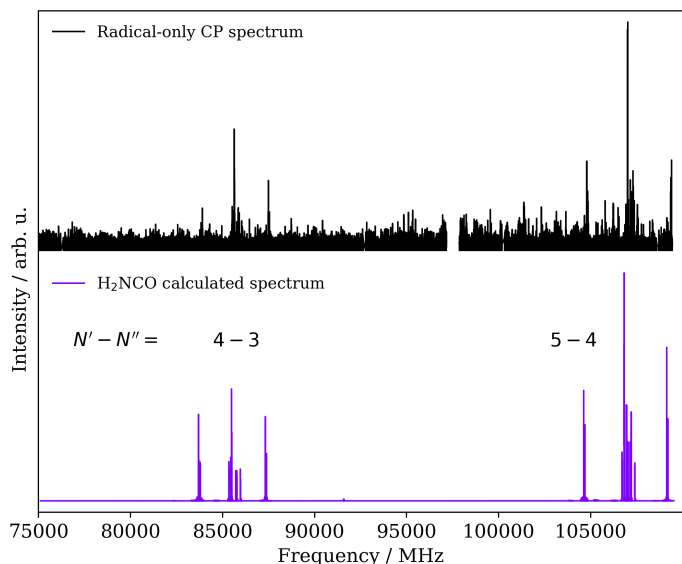


Fig. 3. CP-FTMMW spectrum after data treatment allowing to identify transitions from radical species (top trace) and comparison with predictions for H_2NCO ($\nu = 0$, 300 K) from the quantum chemical calculations performed in this study. The discontinuity on the experimental trace corresponds to a very noisy region that has not been plotted for the sake of clarity.

frequency transitions of the $K_a = 3$ cluster highlighted in orange). These effects, that may reflect high sensitivity of the spin-rotation structure to the magnetic field, are discussed in greater detail in Appendix D. Finally, we observe on the experimental spectrum some transitions that likely arise from vibrational satellites of H_2NCO , as for example the small cluster of transitions around 385 GHz not reproduced by the simulation on Fig. 4. No definite quantum number assignments were performed due to the limited number of observed features (since most of these satellites lie outside the spectral windows scanned in this study). This is explained in greater details in Appendix E.

Once enough a -type transitions were included into the model to ensure its robustness, dedicated searches for weak b -type transitions were undertaken. In total, 34 lines (10 different frequencies) with $K'_a - K''_a = 0 - 1$ are included in the fit. An example of two such b -type transitions, a spin-rotation doublet, is shown in Fig. 5. The asymmetry of the simulated transitions (in particular the higher frequency one) and to some extent of the experimental lines (despite their limited signal-to-noise ratio) is due to the presence of unresolved hyperfine components on the blue side of each transitions, hence creating a weak shoulder on the resulting lines. The inclusion of these b -type transitions in the fit allows for a significant improvement in the determination of the A and Δ_K constants.

Overall, 3588 lines (1441 different frequencies) with $J'' \leq 30$ and $K''_a \leq 12$ have been assigned and included in the fit. The model contains 15 rotational parameters (rotational and centrifugal distortion constants), 6 spin-rotation parameters (including two higher order ones) and 15 hyperfine parameters. To reproduce the observed frequencies at their experimental accuracy, 22 of these parameters have been adjusted while the others were kept fixed at their calculated values. The fit takes a root-mean-square value of 107 kHz and a reduced standard deviation of 0.84. The resulting set of parameters is reported in Table 1 where it is compared to the calculated values. All the adjusted parameters are in excellent agreement with the calculations, with the rotational constants showing relative difference of 0.2 % or

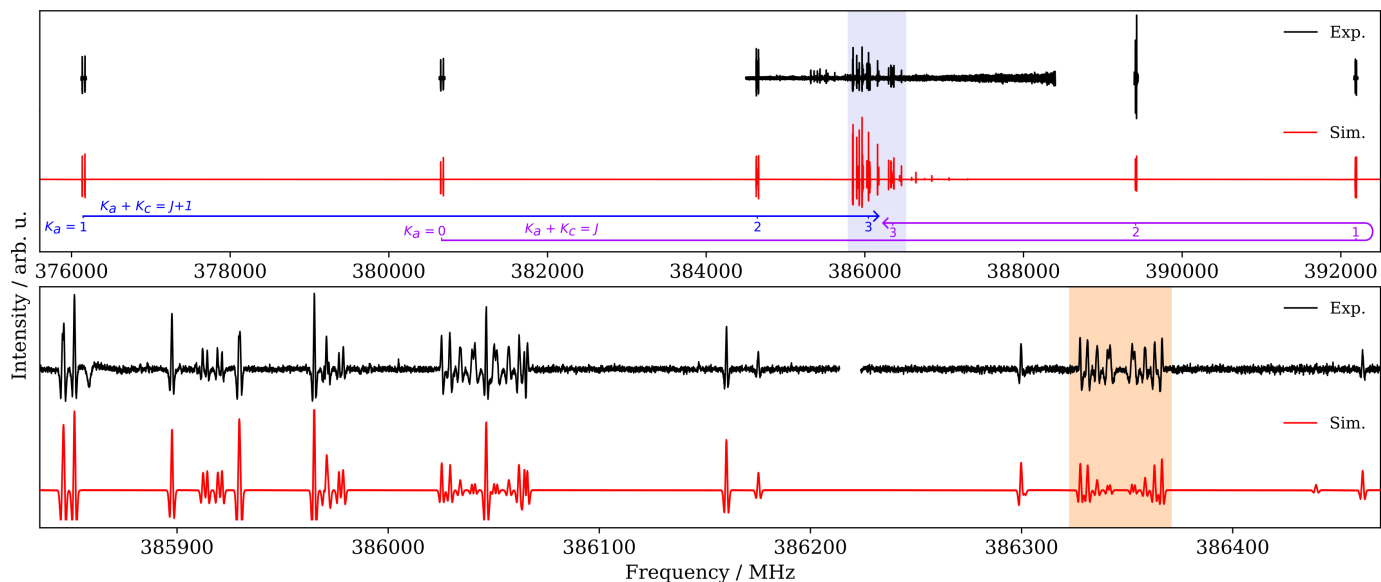


Fig. 4. Overview of the $N' - N'' = 18 - 17$ a -type transition of H₂NCO observed experimentally and comparison with a 300 K simulation obtained using the final spectroscopic constants (Table 1). The lowest K_a values are reported for both asymmetric components on the upper panel (in blue and purple). The lower panel correspond to a zoom into the $K_a = 3 - 12$ region highlighted in light purple in the upper panel. The area highlighted in orange displays partially resolved hyperfine structure ($K_a = 3$). The simulation has been obtained using a Gaussian profile with a full-width-at-half-maximum of 1.3 MHz; the second derivative of the PGOPHER trace is plotted for visual comparison with the experimental spectrum.

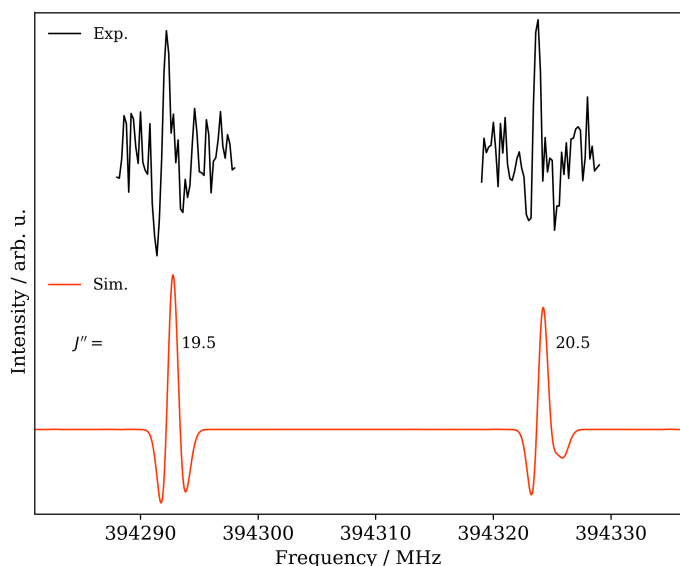


Fig. 5. The $N'_{K_a,K_c} - N''_{K_a,K_c} = 21_{0,21} - 20_{1,20}$ b -type transition of H₂NCO showing two spin-rotation components. The simulation has been obtained using the final spectroscopic constants (Table 1), a 300 K temperature, and a Gaussian profile with a full-width-at-half-maximum of 1.3 MHz; the second derivative of the PGOPHER trace is plotted for visual comparison with the experimental spectrum.

less from the Bayesian-scaled predicted values, and the diagonal quartic centrifugal distortion constants within about 5% of the calculated values. The experimental spin-rotation and hyperfine parameters are not as close to the calculations but close enough that spectral assignments were straightforward.

Using the spectroscopic parameters of H₂NCO derived from this work, reliable predictions can be made up to about 700 GHz (extrapolation to higher frequencies than the experimental measurements can be unreliable, thus prediction above 700 GHz using the present model should be taken with caution). A spectral

catalogue at 300 K (with fully resolved hyperfine structure) is available in the electronic supplementary material together with the assignment and fit files. The catalogue frequencies should be accurate to 100 kHz or better up to 650 GHz, i.e. 1.0 km s⁻¹ at 30 GHz, 0.6 km s⁻¹ at 50 GHz, 0.3 km s⁻¹ at 100 GHz, and 0.1 km s⁻¹ at 350 GHz. It is worth noting that these values may be larger than the linewidths observed in cold interstellar sources below 50 GHz. For instance, TMC-1 linewidths are 0.72 km s⁻¹ around 40 GHz in the QUIJOTE survey (Agúndez et al. 2022). Future experimental work targeting the lowest frequency $K_a = 0$ transitions of H₂NCO ($N = 1 - 0$ around 21.4 GHz, $N = 2 - 1$ around 42.8 GHz, and $N = 3 - 1$ around 64.2 GHz) may help reduce these uncertainties. To help recalculate the catalogue intensities at various temperatures, partition functions have been calculated (from 300 K to 9 K) and are reported in Appendix F.

As final notes, in the course of the present measurements, we observed transitions of carbamyl fluoride (FC(O)NH₂) in the 75–110 GHz region (no higher frequency transitions have been measured due to the open-shell species selectivity of the Zeeman-modulation measurements). The species was previously investigated only in the 16–40 GHz region by Rigden & Jackson (1966); the present measurements and combined fit with the literature data are reported in Appendix G. Lastly, we did not observe transitions that could belong to the HNCHO isomer of H₂NCO. This non-observation can be rationalised by several factors: 1) the lower intensity of HNCHO transitions compared to H₂NCO; 2) the fact that HNCHO may not be synthesised in our experiment; and/or 3) the fact that the transitions of HNCHO could lie outside of the spectral ranges scanned in this study. With respect to point 1, from the spectroscopic information given by the quantum chemical calculations performed in this work (see Appendix H), the lowest energy *cis* conformer of HNCHO possesses dipole moment projections lower than 1 D. Would *cis*-HNCHO be synthesised in concentration similar to H₂NCO, its transitions may thus remain below our detection limit. The *trans* conformer of HNCHO possesses more favourable dipole moment projections (over 2 Debye) but lies

Table 1. Spectroscopic parameters of H₂NCO in the *S*-reduction and relevant fit information. Calculated parameters are compared with those derived from the fit of the experimental measurements. 1 σ error are reported within parentheses in the unit of the last digit; they have been formatted using the PIFORM software developed by [Kisiel \(2001\)](#).

Parameter	units	Calculated ^a	Exp. $\nu = 0$
<i>A</i>	/MHz	126337.24	126264.599(88)
<i>B</i>	/MHz	11145.76	11167.74476(52)
<i>C</i>	/MHz	10242.17	10256.93328(49)
<i>D_N</i>	/kHz	8.043	8.21279(66)
<i>D_{NK}</i>	/kHz	-237.9	-225.0451(79)
<i>D_K</i>	/kHz	9604.	10156.(86)
<i>d₁</i>	/kHz	-1.190	-1.20138(23)
<i>d₂</i>	/kHz	-0.05559	-0.06736(29)
<i>H_N</i>	/Hz	0.01449	0.01410(37)
<i>H_{NK}</i>	/Hz	-0.7904	-0.8267(56)
<i>H_{KN}</i>	/Hz	-54.96	-52.140(56)
<i>H_K</i>	/Hz	2201.	[2201.]
<i>h₁</i>	/Hz	0.005175	[0.005175]
<i>h₂</i>	/Hz	0.0004652	[0.0004652]
<i>h₃</i>	/Hz	0.0001187	[0.0001187]
ϵ_{aa}	/MHz	978.7	871.443(70)
ϵ_{bb}	/MHz	10.52	4.405(10)
ϵ_{cc}	/MHz	-42.69	-40.195(10)
$(\epsilon_{ab} + \epsilon_{ba})/2$	/MHz		-16.207(51)
<i>D_N^s</i>	/kHz		0.0572(60)
<i>D_K^s</i>	/kHz		-189.3(10)
<i>a_F(N)</i>	/MHz	82.37	82.888(55)
$3/2T_{aa}(N)$	/MHz	9.089	8.84(22)
$1/4(T_{bb} - T_{cc})(N)$	/MHz	0.9333	[0.9333]
<i>T_{ab}(N)</i>	/MHz	-4.288	[-4.288]
$3/2\chi_{aa}(N)$	/MHz	3.255	[3.255]
$1/4(\chi_{bb} - \chi_{cc})(N)$	/MHz	1.685	[1.685]
$\chi_{ab}(N)$	/MHz	-0.3841	[-0.3841]
<i>a_F(H₁)</i>	/MHz	76.73	79.863(96)
$3/2T_{aa}(H_1)$	/MHz	3.063	[3.063]
$1/4(T_{bb} - T_{cc})(H_1)$	/MHz	3.153	[3.153]
<i>T_{ab}(H₁)</i>	/MHz	-5.060	[-5.060]
<i>a_F(H₂)</i>	/MHz	-1.067	-2.28(19)
$3/2T_{aa}(H_2)$	/MHz	24.68	24.93(59)
$1/4(T_{bb} - T_{cc})(H_2)$	/MHz	0.7960	[0.7960]
<i>T_{ab}(H₂)</i>	/MHz	1.038	[1.038]
#/ <i>n</i> ^b			3588/1441
<i>N'_{max}, K'_{a max}</i>			31, 12
RMS ^c	/MHz		0.107
σ^d			0.84

^a The calculated *A*, *B*, *C* rotational constants have been Bayesian corrected by a 0.9866 factor (see [Lee & McCarthy 2020](#)), all the other calculated parameters are equilibrium values.

^b Number of lines (#) and number of different frequencies (*n*)

^c Root mean square value

^d Weighted standard deviation

10.5 kJ.mol⁻¹ higher in energy than the *cis*. If thermodynamic factors govern the conformer population under our experimental conditions, much lower concentration of this species may be found, yet again impacting its detectability. Concerning point 2, previous studies have indicated that even though HNCHO should be the most stable isomer, H-abstraction would favour H₂NCO ([Zeng et al. 2023](#)). Regardless, some experimental tests could be performed by using Cl atoms instead of F ones for the H-abstraction, to thus assess whether the halogen nature plays a

role in the favoured site for H-abstraction on the precursor (carbon versus nitrogen atom). Finally, concerning point 3, a previous study has reported the existence of a fast non-planar transition between the *cis* and *trans* conformations of the HNCHO radical that leads to an equilibrium between these configurations ([Andrews 1970](#)). Further high level quantum chemical calculations may be warranted to confirm that point and determine the actual equilibrium geometry of HNCHO, and thus the best predicted rotational constants to perform dedicated search for the species in specific spectral regions.

3.3. Astrochemical implications

To test the new spectroscopic predictions for H₂NCO, we carried out a search for it using the data from the Protostellar Interferometric Line Survey (PILS). PILS is a large spectral survey carried out towards the solar-type protostar IRAS 16293–2422 with the Atacama Large millimetre/submillimetre Array (ALMA) 12 m array and the Atacama Compact Array (ACA) in band 7. It has a spatial resolution of $\sim 0.5''$ and a sensitivity of 4–5 mJy beam⁻¹ for a bin width of 1 km s⁻¹ ([Jørgensen et al. 2016](#)). This survey, which covers the spectral range 329–363 GHz, has led to several new molecular detections in low-mass protostars (e.g., [Lykke et al. 2017](#); [Ligterink et al. 2017](#); [Fayolle et al. 2017](#); [Coutens et al. 2018, 2019](#); [Manigand et al. 2021](#)). Formamide and several of its isotopologues (NHDCO, NH₂CDO, NH₂¹³CHO) were detected at a position located one beam offset from the continuum peak position of the B component (IRAS16293 B in the following; [Coutens et al. 2016](#)). Cyanamide (H₂NCN) was also detected towards the same position ([Coutens et al. 2018](#)). A search for the H₂NCO radical is consequently pertinent towards this source.

Local thermodynamic equilibrium (LTE) models were produced with the CASSIS¹ software and compared to the spectrum extracted at the same position as the previous molecular studies. The models assume a linewidth of 1 km s⁻¹, a source size of 0.5'' and a v_{LSR} of 2.7 km s⁻¹, and take into account the total partition function given in Appendix F. The excitation temperatures of complex organic molecules vary in this source between ~ 125 K and 300 K ([Jørgensen et al. 2018](#)). Different excitation temperatures were consequently assumed in the search, but independent on the assumed temperature no detected lines could be claimed above noise of the observed spectrum. We used the brightest H₂NCO lines predicted by the models that are not contaminated by emission of other molecules to derive upper limits on the column density, namely the *a*-type, *R*-branch transitions involving $N''_{K''_a, K''_c} = 15_{5,10/11}$ (both spin-rotation components around 342.957 and 343.059 GHz), 16_{1,16}} (around 355.358 and 355.393 GHz), 16_{1,16}} (around 359.950 and 359.981 GHz), and $N''_{K''_a, K''_c}(J'') = 15_{6,9/10}(15.5)$ (around 343.109 GHz). Based on the transitions at 342.957, 343.059 and 343.109 GHz, the upper limit is estimated to be about 1.7×10^{14} cm⁻² if the excitation temperature is similar to NH₂CHO (~ 300 K, [Coutens et al. 2016](#)). For a lower excitation temperature of ~ 125 K, we used the groups of transitions at 355.358, 355.393, 359.950, and 359.981 GHz and found a very close upper limit of 8.0×10^{13} cm⁻². These non-detected lines are shown in Figure 6.

[Coutens et al. \(2016\)](#) found column densities of NH₂CHO and HNCO equal to 1.0×10^{16} and 2.7×10^{16} cm⁻², respectively, using their ¹³C isotopologue lines and a ¹²C/¹³C ratio

¹ CASSIS has been developed by IRAP-UPS/CNRS ([Vastel et al. 2015](#)), <http://cassis.irap.omp.eu>

of 68 (Milam et al. 2005). H₂NCO is consequently ≥ 60 times less abundant than NH₂CHO and ≥ 160 than HNC towards IRAS16293 B. The radical NCO has never been searched towards IRAS 16293–2422 as far as we know. We searched for it in the PLS data but we only derived an upper limit of 7×10^{14} cm⁻² for $T_{\text{ex}} = 300$ K and 5×10^{14} cm⁻² for $T_{\text{ex}} = 125$ K. Among the other NCO-bearing molecules detected in IRAS16293B, CH₃NCO has a column density of $\sim 3\text{--}4 \times 10^{15}$ cm⁻² (Ligterink et al. 2017; Martín-Doménech et al. 2017) and is at least 17 times more abundant than H₂NCO. Acetamide (CH₃C(O)NH₂) has also been tentatively detected by Ligterink et al. (2018b) with a column density of $(9\text{--}25) \times 10^{14}$ cm⁻² depending on the excitation temperature. If confirmed, it would mean that this molecule is $\geq 5\text{--}15$ times more abundant than H₂NCO.

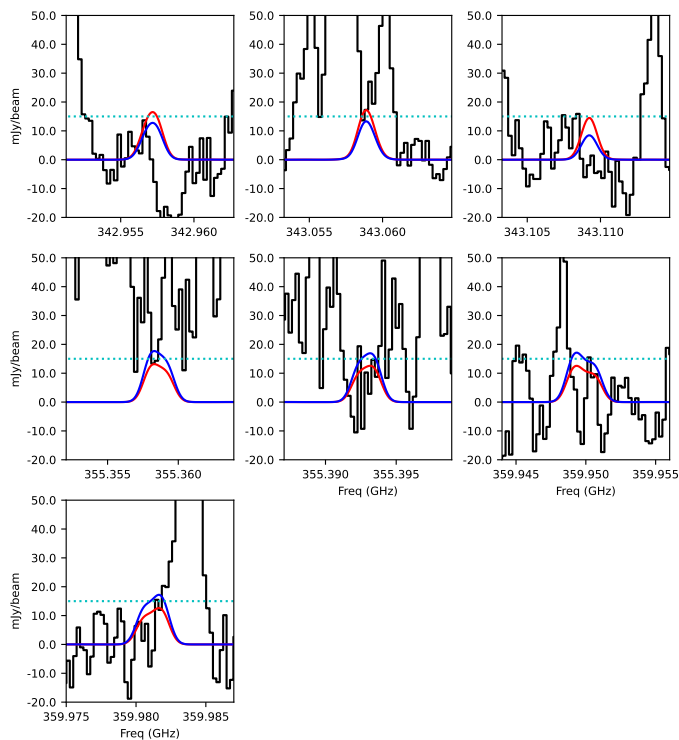


Fig. 6. Undetected transitions of H₂NCO that were used to determine the column density upper limits. The ALMA observed spectrum of IRAS16293 B is in black. The LTE model for $T_{\text{ex}} = 300$ K is in red, while the one for $T_{\text{ex}} = 125$ K is in blue. The dotted cyan line corresponds to the 3 rms level per 1 km s⁻¹, 1 km s⁻¹ being the typical line width at this position.

To understand the astrophysical implications of the non-detection of H₂NCO in IRAS16293 B we compare the upper limit derived above to the calculated abundance obtained using the model used in Coutens et al. (2022); Manigand et al. (2021) which uses the Nautilus code (Ruaud et al. 2016)—a 3-phase gas, dust grain ice surface, and dust grain ice mantle time dependent chemical model employing kida.uva.2014 (Wakelam et al. 2015) as the basic reaction network. The model was recently updated to better describe iCOMs on grains and in the gas-phase (800 individual species are included in the network and are involved in 9000 separate reactions, Coutens et al. 2022; Manigand et al. 2021). The physical model to describe IRAS16293 B evolution consists in the two successive evolutionary stages of a low-mass protostar: a uniform and constant stage corresponding to the pre-stellar phase, or the cold-core phase, followed (after 1×10^6 years) by a collapse phase as described in Manigand

et al. (2021). The following conditions are used in the pre-stellar phase: homogeneous gas with a density equal to 2.5×10^4 cm⁻³; temperature of 10 K for both gas and dust; visual extinction of 10 mag; cosmic-ray ionisation rate of 1.3×10^{-17} s⁻¹; standard external UV field of 1 G₀; and the same initial abundances than in Manigand et al. (2021).

The evolution of the abundances during the cold-core phase and the collapse phase is shown in Figure 7. H₂NCO and the species directly related to it, HNC and NH₂CHO, are mostly produced on grain surfaces and the closed shell species HNC and NH₂CHO are released in the gas-phase when the temperature reaches the desorption temperature, between 120 to 130 K—the binding energy of HNC is measured equal to 3900 K (Noble et al. 2015) and that of NH₂CHO is between 5056 and 6990 K (Chaabouni et al. 2018). More precisely, in our network HNC is mainly produced by the reaction s-N + s-HCO, where s- means species on grain. This reaction is effective even at 10 K in the cold-core phase as N is, along with atomic hydrogen, relatively mobile on grains when we consider its adsorption energy equal to 700 K (Molpeceres et al. 2020; Shimonishi et al. 2018) and $E_{\text{diffusion}} = 0.4 \times E_{\text{binding}}$ (Hasegawa et al. 1992). H₂NCO is produced by hydrogenation of HNC (which presents a barrier but is made possible by tunnelling), H-atom abstraction from s-NH₂CHO and also by the s-CN + s-H₂O reaction, which according to a recent theoretical study is possible by a concerted effect of water molecules in the ice (Rimola et al. 2018). Finally, NH₂CHO is produced by the hydrogenation of H₂NCO and by the s-NH₂ + s-HCO reaction. The agreement between the modelled abundances for HNC and NH₂CHO and the observations for IRAS16293 B (and also molecular clouds for HNC) is relatively good, given the many uncertainties and unknowns (for example the branching ratios between the s-NH₂CHO and s-NH₃ + s-CO pathways for the s-H + s-H₂NCO reaction).

Figure 7 also shows that the calculated abundance of s-H₂NCO is high as long as the temperature does not exceed 25 K. Above this temperature, certain radicals become mobile on ice—s-HCO, for example, has a relatively low binding energy around 3000 K (Enrique-Romero et al. 2016; Minissale et al. 2016; Sameera et al. 2017; Wakelam et al. 2017), but not H₂NCO, whose binding energy is calculated to be around 7000 K (Wakelam et al. 2017). Then, as the s-radical + s-radical reaction are barrierless, the radicals will react with each other on the grains before being able to desorb. Note that as the diffusion energy of the radicals is always notably lower than the binding energy ($E_{\text{diffusion}} = 0.4 \times E_{\text{binding}}$ in our model), the radicals will diffuse before desorbing and will therefore be rapidly destroyed on the grains before they can be injected into the gas phase. The only possibility for radicals to desorb is if they are produced at temperatures above their desorption temperature, as in the case of NO, or possibly HCO, detected in IRAS16293 B (Ligterink et al. 2018a; Rivilla et al. 2019). The non-detection of H₂NCO suggests that this radical is not produced at high temperature on grains nor is it produced efficiently in the protostellar hot gas phase. However, its non-detection does not compromise its important role as an intermediate in NH₂CHO production.

4. Conclusions

We have conducted an extensive investigation into the room-temperature pure rotational spectrum of the H₂NCO radical (previously never detected in the gas phase in the laboratory) in the 75–660 GHz region. Close to 1500 frequencies have been assigned in $v = 0$, upon guidance from quantum-chemical calculations, enabling a robust set of spectroscopic parameters to

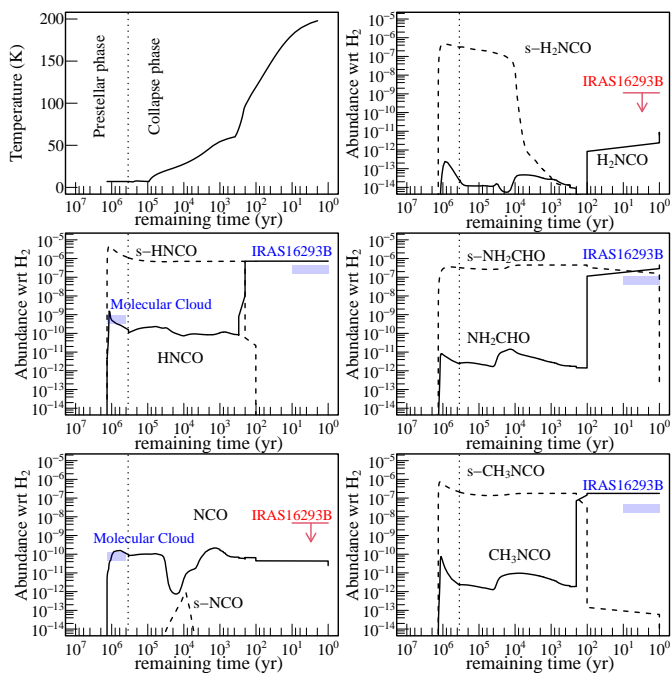


Fig. 7. Time evolution of the temperature and the abundances (with respect to molecular hydrogen) in the gas phase (solid lines) and on the grain surface (dashed) of HNCO , H_2NCO , NH_2CHO , NCO , and CH_3NCO species during the cold-core phase and the collapse phase. The time axis is reversed to better visualise the abundances evolution. The observed gas-phase abundances are indicated in blue. Detection in IRAS16293 B are from Coutens et al. (2016); Hernández-Gómez et al. (2018); Martín-Doménech et al. (2017) for HNCO and from Coutens et al. (2016); Jørgensen et al. (2020); Martín-Doménech et al. (2017) for NH_2CHO . Detection in dense molecular clouds are from Marcelino et al. (2018b, 2009) and Turner et al. (1999). The upper limit for the relative abundance of gas phase H_2NCO and NCO in IRAS16293 B are shown in red. The observed abundances for IRAS16293 B are calculated from the observed column densities using an H_2 column density equal to $1.5 \times 10^{23} \text{ cm}^{-2}$ so that the chemical model reproduces the observed abundance of CH_3OH (this is equivalent to using abundances relative to CH_3OH).

be derived for the species. Using this model, accurate spectral predictions can be made over the entire millimetre- and submillimetre-wave spectral regions. This opens up the possibility for interstellar searches for the radical in cold to warm environments ($T \leq 300 \text{ K}$). Searches have been undertaken toward IRAS16293 B, a source where the related molecule NH_2CHO is abundant, using the PILS survey. No transition of the radical was detected and upper limits on the column densities have been derived. The absence of detection of H_2NCO in the gas phase is consistent with a physico-chemical model of the formation of complex molecules during the earliest stages of the source.

Acknowledgements. This work has been supported by the *Région Ile-de-France*, through DIM-ACAV⁺, the *Agence Nationale de la Recherche* (ANR-19-CE30-0017-01), the “*Investissements d’Avenir*” LabEx PALM (ANR-10-LABX-0039-PALM), and the *Programme National “Physique et Chimie du Milieu Interstellaire”* (PCMI) of CNRS/INSU with INC/INP co-funded by CEA and CNES. Quantum chemical calculations were performed using HPC resources from the “*Mésocentre*” computing centre of CentraleSupélec and École Normale Supérieure Paris-Saclay supported by CNRS and Région Île-de-France (<http://mesocentre.centralesupelec.fr/>). This paper makes use of the following ALMA data: ADS/JAO.ALMA#2013.1.00278.S. ALMA is a partnership of ESO (representing its member states), NSF (USA) and NINS (Japan), together with NRC (Canada) and NSC and ASIAA (Taiwan), in cooperation with the Republic of Chile. The Joint ALMA Observatory is operated by ESO, AUI/NRAO and NAOJ. A. C. received financial support from the European Research Council

(ERC) under the European Union’s Horizon 2020 research and innovation programme (ERC Starting Grant “Chemtrip”, grant agreement No 949278). J.K.J. acknowledges support from the Independent Research Fund Denmark (grant number 0135-00123B). We thank T. Huet for the loan of the audio-amplifier and M. Goubet, Z. Kisiel, M. D. Marshall, and B. J. Esselman for useful discussion regarding the vibration-rotation calculations with Gaussian.

References

- Agarwal, V. K., Schutte, W., Greenberg, J. M., et al. 1985, *Origins Life Evol Biosphere*, 16, 21
- Agúndez, M., Marcelino, N., Cabezas, C., et al. 2022, *Astron. Astrophys.*, 657, A96
- Alonso, E. R., Kolesníková, L., Belloche, A., et al. 2021, *A&A*, 647, A55
- Andrews, P. 1970, *J. Mol. Struct.*, 6, 85
- Belloche, A., Garrod, R. T., Müller, H. S. P., et al. 2019, *A&A*, 628, A10
- Bisschop, S. E., Fuchs, G. W., Van Dishoeck, E. F., & Linnartz, H. 2007, *A&A*, 474, 1061
- Bredelhöft, J. H., Böhrer, E., Schmidt, F., Borrmann, T., & Swiderek, P. 2017, *ACS Earth Space Chem.*, 1, 50
- Buchanan, Z., Lee, K. L. K., Chitarra, O., et al. 2021, *J. Mol. Spectrosc.*, 377, 111425
- Cernicharo, J., Kisiel, Z., Tercero, B., et al. 2016, *A&A*, 587, L4
- Chaabouni, H., Diana, S., Nguyen, T., & Dulieu, F. 2018, *A&A*, 612, A47
- Chahbazian, R., Martin-Drumel, M.-A., & Pirali, O. 2024, *J. Phys. Chem. A*, 128, 370
- Chai, J.-D. & Head-Gordon, M. 2008, *Phys. Chem. Chem. Phys.*, 10, 6615
- Chitarra, O., Martin-Drumel, M.-A., Gans, B., et al. 2020, *A&A*, 644, A123
- Chitarra, O., Pirali, O., Spaniol, J.-T., et al. 2022, *J. Phys. Chem. A*, 126, 7502
- Coudert, L. H., Chitarra, O., Spaniol, J.-T., et al. 2022, *J. Chem. Phys.*, 156, 244301
- Coutens, A., Jørgensen, J. K., Van Der Wiel, M. H. D., et al. 2016, *A&A*, 590, L6
- Coutens, A., Ligterink, N. F. W., Loison, J. C., et al. 2019, *A&A*, 623, L13
- Coutens, A., Loison, J.-C., Boulanger, A., et al. 2022, *A&A*, 660, L6
- Coutens, A., Willis, E. R., Garrod, R. T., et al. 2018, *A&A*, 612, A107
- Dunning, T. H. 1989, *J. Chem. Phys.*, 90, 1007
- Endres, C. P., Schlemmer, S., Schilke, P., Stutzki, J., & Müller, H. S. 2016, *J. Mol. Spectrosc.*, 327, 95
- Enrique-Romero, J., Rimola, A., Ceccarelli, C., & Balucani, N. 2016, *MNRAS: Letters*, 459, L6
- Fayolle, E. C., Öberg, K. I., Jørgensen, J. K., et al. 2017, *Nature Astronomy*, 1, 703
- Förstel, M., Maksyutenko, P., Jones, B. M., et al. 2016, *Chem. Commun.*, 52, 741
- Fox, W. M. & Smith, P. 1968, *J. Chem. Phys.*, 48, 1868
- Frisch, M. J., Trucks, G. W., Schlegel, H. B., et al. 2016, *Gaussian 16 Revision A.01*
- Garrod, R. T., Jin, M., Matis, K. A., et al. 2022, *ApJS*, 259, 1
- Gorai, P., Bhat, B., Sil, M., et al. 2020, *ApJ*, 895, 86
- Gordy, W. & Cook, R. L. 1984, *Microwave molecular spectra*, 3rd edn., *Techniques of chemistry* No. v. 18 (New York: Wiley)
- Gupta, H., Gottlieb, C. A., Lattanzi, V., Pearson, J. C., & McCarthy, M. C. 2013, *ApJ*, 778, L1
- Halfen, D. T., Ilyushin, V. V., & Ziurys, L. M. 2015, *ApJ*, 812, L5
- Hasegawa, T. I., Herbst, E., & Leung, C. M. 1992, *ApJS*, 82, 167
- Haupa, K. A., Tarczay, G., & Lee, Y.-P. 2019, *J. Am. Chem. Soc.*, 141, 11614
- Hernández-Gómez, A., Loinard, L., Caux, E., et al. 2018, *MNRAS*, 483, 2014
- Hubbard, J. S., Voecks, G. E., Hobby, G. L., et al. 1975, *J. Mol. Evol.*, 5, 223
- Jørgensen, J. K., Müller, H. S. P., Calcutt, H., et al. 2018, *A&A*, 620, A170
- Jørgensen, J. K., van der Wiel, M. H. D., Coutens, A., et al. 2016, *A&A*, 595, A117
- Jørgensen, J. K., Belloche, A., & Garrod, R. T. 2020, *Annual Review of Astronomy and Astrophysics*, 58, 727
- Kawaguchi, K., Saito, S., & Hirota, E. 1985, *Mol. Phys.*, 55, 341
- Kisiel, Z. 2001, *Assignment and Analysis of Complex Rotational Spectra*, ed. J. Demaison, K. Sarka, & E. A. Cohen (Dordrecht: Springer Netherlands), 91–106
- Kolesníková, L., Belloche, A., Koucký, J., et al. 2022, *A&A*, 659, A111
- Lee, K. L. K. & McCarthy, M. 2020, *J. Phys. Chem. A*, 124, 898
- Ligterink, N. F. W., Ahmadi, A., Luitel, B., et al. 2022, *ACS Earth Space Chem.*, 6, 455
- Ligterink, N. F. W., Calcutt, H., Coutens, A., et al. 2018a, *A&A*, 619
- Ligterink, N. F. W., Coutens, A., Kofman, V., et al. 2017, *MNRAS*, 469, 2219
- Ligterink, N. F. W., Terwisscha van Scheltinga, J., Taquet, V., et al. 2018b, *MNRAS*, 480, 3628
- Livingston, R. & Zeldes, H. 1967, *J. Chem. Phys.*, 47, 4173
- López-Sepulcre, A., Jaber, A. A., Mendoza, E., et al. 2015, *MNRAS*, 449, 2438

- Lykke, J. M., Coutens, A., Jørgensen, J. K., et al. 2017, *A&A*, 597, A53
- Manigand, S., Coutens, A., Loison, J. C., et al. 2021, *A&A*, 645, A53
- Marcelino, N., Agúndez, M., Cernicharo, J., Roueff, E., & Tafalla, M. 2018a, *A&A*, 612, L10
- Marcelino, N., Agúndez, M., Cernicharo, J., Roueff, E., & Tafalla, M. 2018b, *A&A*, 612, L10
- Marcelino, N., Cernicharo, J., Tercero, B., & Roueff, E. 2009, *ApJ*, 690, L27
- Martín-Doménech, R., Rivilla, V. M., Jiménez-Serra, I., et al. 2017, *MNRAS*, 469, 2230
- Martin-Drumel, M.-A., Spaniol, J.-T., Hölzel, H., et al. 2023, *Faraday Discuss.*, 245, 284
- Martín-Doménech, R., Rivilla, V. M., Jiménez-Serra, I., et al. 2017, *MNRAS*, 469, 2230
- McKean, D. C., Craig, N. C., & Law, M. M. 2008, *J. Phys. Chem. A*, 112, 6760
- Milam, S. N., Savage, C., Brewster, M. A., Ziurys, L. M., & Wyckoff, S. 2005, *ApJ*, 634, 1126
- Miller, J. A. & Melius, C. F. 1992, *Int. J. Chem. Kinet.*, 24, 421
- Minissale, M., Dulieu, F., Cazaux, S., & Hocuk, S. 2016, *A&A*, 585, A24
- Molpeceres, G., Zaverkin, V., & Kästner, J. 2020, *MNRAS*
- Nagy, B., Csontos, J., Kállay, M., & Tasi, G. 2010, *J. Phys. Chem. A*, 114, 13213
- Nguyen, M. T., Sengupta, D., Vereecken, L., Peeters, J., & Vanquickenborne, L. G. 1996, *J. Phys. Chem.*, 100, 1615
- Noble, J. A., Theule, P., Congiu, E., et al. 2015, *A&A*, 576, A91
- Pettersson, M., Khriachtchev, L., Jolkkonen, S., & Rasanen, M. 1999, *J. Phys. Chem. A*, 103, 9154
- Pickett, H. M. 1991, *J. Mol. Spectrosc.*, 148, 371
- Poskrebyshev, G. A. 2015, *Kinet Catal*, 56, 245
- Poskrebyshev, G. A. 2017, *Comput. Theor. Chem.*, 1118, 81
- Raunier, S., Chiavassa, T., Duvernay, F., et al. 2004, *A&A*, 416, 165
- Rigden, J. S. & Jackson, R. H. 1966, *J. Chem. Phys.*, 45, 3646
- Rimola, A., Skouteris, D., Balucani, N., et al. 2018, *ACS Earth and Space Chemistry*
- Rivilla, V. M., Beltrán, M. T., Vasyunin, A., et al. 2019, *MNRAS*, 483, 806
- Rodríguez-Almeida, L. F., Rivilla, V. M., Jiménez-Serra, I., et al. 2021, *A&A*, 654, L1
- Ruaud, M., Wakelam, V., & Hersant, F. 2016, *MNRAS*, 459, 3756
- Sameera, W. M. C., Senevirathne, B., Andersson, S., Maseras, F., & Nyman, G. 2017, *J. Phys. Chem. C*, 121, 15223
- Shapley, W. A. & Bacskay, G. B. 1999, *J. Phys. Chem. A*, 103, 4505
- Shimonishi, T., Nakatani, N., Furuya, K., & Hama, T. 2018, *ApJ*, 855, 27
- Slate, E. C. S., Barker, R., Euesden, R. T., Revels, M. R., & Meijer, A. J. H. M. 2020, *MNRAS*, 497, 5413
- Smith, P. & Wood, P. B. 1966, *Can. J. Chem.*, 44, 3085
- Song, L. & Kästner, J. 2016, *Phys. Chem. Chem. Phys.*, 18, 29278
- Turner, B. E., Terzieva, R., & Eric, H. 1999, *ApJ*, 518, 699
- Vastel, C., Bottinelli, S., Caux, E., Glorian, J. M., & Boiziot, M. 2015, in *SF2A-2015: Proceedings of the Annual meeting of the French Society of Astronomy and Astrophysics*, 313–316
- Wakelam, V., Loison, J. C., Herbst, E., et al. 2015, *ApJS*, 217, 20
- Wakelam, V., Loison, J. C., Mereau, R., & Ruaud, M. 2017, *Molecular Astrophysics*, 6, 22
- Western, C. M. 2017, *J. Quant. Spectr. Rad. Transf.*, 186, 221
- Woon, D. E. & Dunning, T. H. 1993, *J. Chem. Phys.*, 98, 1358
- Yonezawa, T., Noda, I., & Kawamura, T. 1968, *Bull. Chem. Soc. Jpn.*, 41, 766
- Yonezawa, T., Noda, I., & Kawamura, T. 1969, *Bull. Chem. Soc. Jpn.*, 42, 650
- Zeng, S., Rivilla, V. M., Jiménez-Serra, I., et al. 2023, *MNRAS*, 523, 1448

Appendix A: Additional calculation outputs

Table A.1. Fundamental modes of H₂NCO calculated in this study (ω B97X-D/cc-pVQZ). Energies are reported in cm⁻¹ and intensities in km mol⁻¹.

Mode	$E(\text{harm})$	$E(\text{anharm})$	$I(\text{harm})$	$I(\text{anharm})$	Sym.
ν_1	3754	3615	71.83	59.41	A'
ν_2	3556	3401	11.46	3.85	A'
ν_3	1895	1874	341.28	305.02	A'
ν_4	1617	1576	61.12	39.26	A'
ν_5	1249	1222	58.97	42.03	A'
ν_6	1106	1099	0.30	0.05	A'
ν_7	540	533	6.29	27.21	A'
ν_8	631	601	0.47	0.58	A''
ν_9	282	422	204.63	146.52	A''

Table A.2. Calculated α values (in MHz) for H₂NCO in excited vibrational states (ω B97X-D/cc-pVQZ). Predictions of the rotational constants values in $\nu_i = 1$ can be retrieved using the formula $B_i = B_0 + \alpha_{B_i}$.

State	α_A	α_B	α_C
$\nu_1 = 1$	-167.0	-17.3	-14.1
$\nu_2 = 1$	-324.0	-12.6	-12.1
$\nu_3 = 1$	-1483.3	-33.1	-33.3
$\nu_4 = 1$	816.1	4.7	-13.4
$\nu_5 = 1$	1397.9	-55.2	-51.4
$\nu_6 = 1$	1016.2	-5.4	-27.8
$\nu_7 = 1$	-3491.4	-14.7	-4.4
$\nu_8 = 1$	4879.1	-1.3	0.1
$\nu_9 = 1$	-3714.2	-23.9	11.6

Appendix B: Initial searches for radical products using the chirped-pulse spectrometer

As mentioned in section 2.3, we performed initial searches for H-abstraction products from formamide using the chirped-pulse spectrometer because it ideally allows to rapidly, and repeatedly, scan a broad spectral region under various experimental conditions. The initial searches were performed using a 0.5 μ s excitation pulse which was found to give reasonably good signal for both strong and moderate dipole moment transitions, in order to scan without bias for potential reaction products in our experiment. Starting with a pressure found to maximize the signal of formamide in our flow conditions (5 μ bar), we recorded several chirped-pulse spectra for formamide:F₂/He ratio of 1:0.5, 1:1, 1:2, and 1:3. Each of these spectra was recorded for about 1 hour (500,000 averages) and the measurement was repeated after placing a permanent magnet below the cell. Before recording the spectra, we ensured that the added pressure of F₂/He did not degrade the signal of the precursor (as high pressure can cause the polarized molecules to relax faster by collision hence yielding shortened FIDs).

Because the experimental conditions were relatively stable during the scans, and because the magnet does not affect the signal of the precursor lines nor that of the close-shell products of the reaction, it was possible to essentially subtract the spectrum recorded with the magnet from the one recorded without it for each formamide:F₂/He pressure ratio. By doing so, only transitions whose intensity are affected by the magnetic field appear on

the resulting spectrum. Concretely, because chirped-pulse spectra display some negative noise and spurs, and because there was some slight variations in the line intensity of the precursor, special care was taken in the subtraction procedure in order to not add positive noise to the subtracted spectrum and to filter all signal from the precursor. To do so, all negative intensity points on the spectrum recorded with the magnet are set to zero. Then, for each frequency point, the resulting intensity from this treated spectrum is multiplied by a constant factor (typically 1 to 1.2, to account for intensity fluctuations of the precursor signal) and subtracted from the corresponding intensity on the spectrum recorded without magnet. To enable a straightforward display of the subtracted spectrum, a negative intensity cut-off is applied for values below the noise level. Finally, remaining spurious signals are identified by visual inspection of the subtracted spectrum and discarded (intensity set to zero), as are some particularly noisy regions of the spectrum (typically with our instrument the region around 97.5 GHz is extremely noisy).

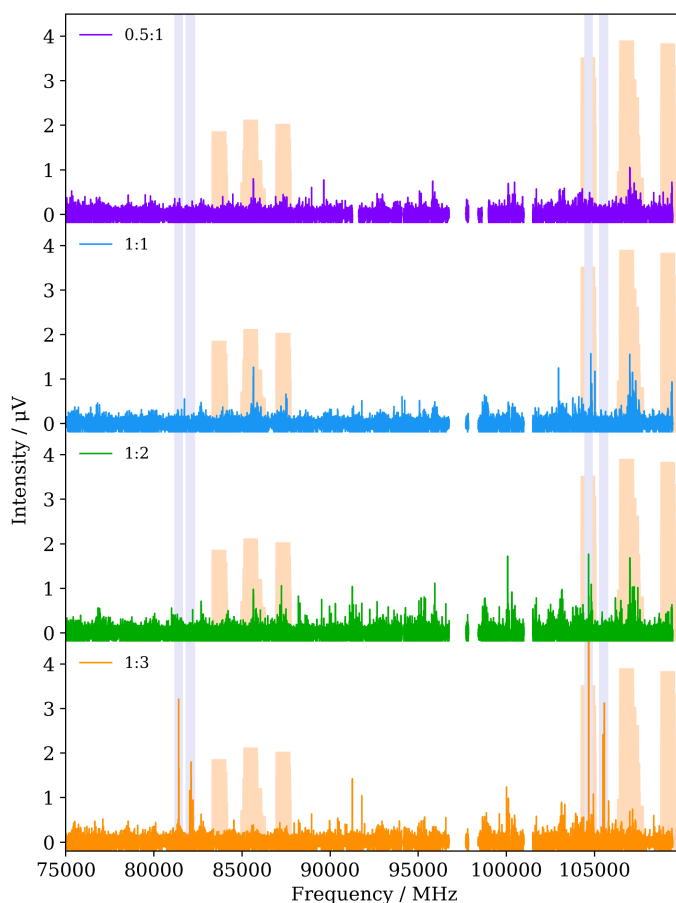


Fig. B.1. Comparison of the different CP spectra after data treatment allowing to identify transitions from radical species (formamide:F₂/He pressure ratio of 1:0.5, 1:1, 1:2, and 1:3, from top to bottom). The shaded areas correspond to ± 200 MHz windows around the spectral predictions from the NCO and H₂NCO radicals (in light blue and orange, respectively). For NCO, predictions are from the CDMS database (Endres et al. 2016) based on the experimental work by Kawaguchi et al. (1985). For H₂NCO, calculated values are from this work and the relative intensity is proportional to the expected line intensity at 300 K, in arbitrary units. Discontinuities on the experimental spectra correspond to very noisy regions that have not been plotted for the sake of clarity.

Overall, this procedure allows us to search for transitions arising from radical species on each spectrum. Fig. B.1 shows

the resulting spectra. Around the areas where transitions of H₂NCO are expected, features are easily distinguishable on all spectra; they are the strongest on the 1:1 and 1:2 ratio spectra. The only other radical clearly identifiable on the spectra is NCO, which presents strong transitions on the 1:3 ratio spectrum. The experimental data do not allow for a comparison of the production of the two radicals in terms of concentration because of both the different polarisation of the two radicals (which depends on their dipole moment projections) and the respective volume where they are present (which depends on the lifetime/reactivity of each species). We, however, qualitatively see here that a high concentration of F atoms yields multiple H-abstraction from formamide. As a final note, transitions of H₂NCO are more than 1000 times weaker than transitions of formamide on the CP spectra, thus the identification of the radical features was only possible because the precursor spectral density was not too large, allowing for transitions of H₂NCO to lie in transparency windows. The methodology used in the present study would not be applicable for a precursor presenting a very dense spectrum in the W-band region.

Following identification of H₂NCO on these spectra, experimental conditions were optimised to maximise the signal of this radical. A pulse length of 0.25 μs was found to maximise the signal of the observed *a*-type transitions, as expected from the relatively large projected dipole moment of 3.7 Debye. Long acquisitions were subsequently undertaken, ultimately yielding a 2.9 million averaged FIDs spectrum. The procedure enabling to retrieve a radical-only spectrum was applied to that spectrum, the resulting spectrum is displayed in Fig. 3 of the main text and a zoom onto the $N'_{K'_a, K'_c} - N''_{K''_a, K''_c} = 5_{0,5} - 4_{0,4}$ is shown on Fig. B.2.

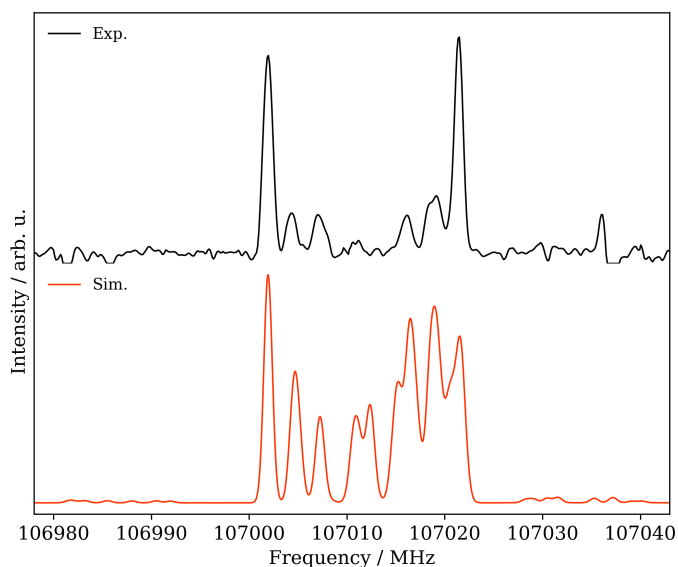


Fig. B.2. Experimental CP spectrum in the 107 GHz region where the $N'_{K'_a, K'_c} - N''_{K''_a, K''_c} = 5_{0,5} - 4_{0,4}$ *a*-type transition of H₂NCO lies, and comparison with a simulation obtained with PGOPHER using the final set of spectroscopic parameters (see Table 1), a 300 K temperature, and a Gaussian profile with a full-width-at-half-maximum of 1 MHz.

Other species synthesised On the final CP spectrum, many close-shell molecules synthesised in the experiment are visible. We observe notably strong lines of HCN (including transitions in $\nu_2 = 1$ and $\nu_3 = 1$, and of the H¹³CN and HC¹⁵N species), HNC, HNCO (including strong vibrational satellites and both ¹³C and

¹⁵N isotopologues), as well as lines of fluorinated species HFCO, FC(O)NH₂, F₂CO, and FCN (in $\nu = 0$, $\nu_2 = 1$). Transitions of FC(O)NH₂ are observed for the first time in the 75–110 GHz spectral region, see Appendix G for additional information.

Appendix C: Hyperfine structure and fit detail

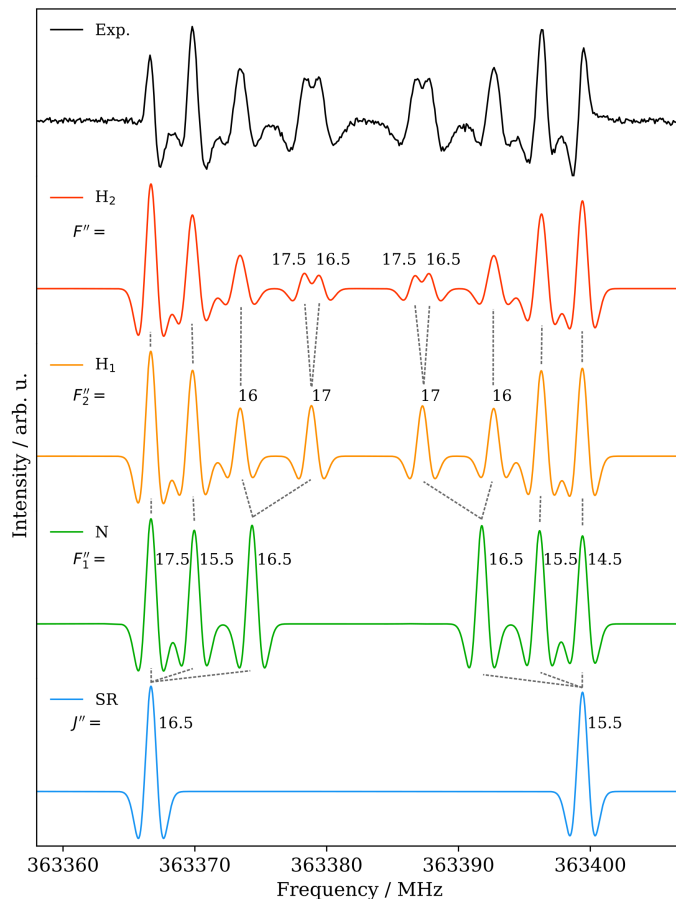


Fig. C.1. Evolution of the structure of the $N'_{K'_a, K'_c} - N''_{K''_a, K''_c} = 17_{2,16} - 16_{2,15}$ transition of H₂NCO upon consideration of the spin-rotation (SR) and hyperfine structures (N, H₁, and H₂), and comparison with the experimental spectrum. The quantum numbers of the different components are reported (unresolved values are omitted). The various simulations have been obtained the final spectroscopic constants (Table 1), a 300 K temperature, and a Gaussian profile with a full-width-at-half-maximum of 1.3 MHz; the second derivative of the PGOPHER traces is plotted for visual comparison with the experimental spectrum.

As mentioned in the main text, many transitions present a resolved hyperfine structure as illustrated in Fig. C.1 where the experimental spectrum of the $N'_{K'_a, K'_c} - N''_{K''_a, K''_c} = 17_{2,16} - 16_{2,15}$ transition is compared to simulation of the fine structure (*J* quantum number) and successive hyperfine structures (*F*₁, *F*₂, *F* quantum numbers). On this transition, the central frequency components show a fully resolved hyperfine structure while the lowest and highest frequency components lie essentially at the frequency of nitrogen-hyperfine-split components. Special care was taken to include these components in the fit. To limit the number of lines in the fit, we have introduced two dummy vibrational states in the model (i.e., at the same energy as $\nu = 0$), accounting for various cases of resolved hyperfine structure. The fully resolved hyperfine structure corresponds to $\nu = 0$ (red trace on Fig. C.1). For

this state, all the parameters from Table 1 are included. Transitions displaying only N and H₁ hyperfine structure (orange trace on Fig. C.1) are coded as $\nu = 1$; the hyperfine parameters pertaining to H₂ are omitted. Finally, transitions only showing a N-resolved hyperfine structure (green trace on Fig. C.1) are coded as $\nu = 2$; the hyperfine parameters pertaining to both H₁ and H₂ are omitted. However, the hyperfine splitting is often asymmetrical with respect to the unsplit transition. A striking example is visible on Fig. C.1 for the $F''_1 = 16.5 \rightarrow F''_2$ transitions but to some extent this also affects the $F''_1 = 15.5 \rightarrow F''_2$ transitions. Thus, particular care was taken in the choice of the hyperfine-case for the assignment. Concretely, an unresolved-case was only chosen if it did not induce a significant frequency shift for the transition.

Finally, Fig. C.1 also illustrates the asymmetry in line profile observed for many transitions recorded by Zeeman-modulation spectroscopy, here the lowest and highest frequency components of the transition that exhibit a shape closer to that of a second derivative. This effect has been investigated in greater detail in Appendix D.

Appendix D: Line profile in Zeeman modulation

In the course of our measurements by Zeeman-modulation spectroscopy, we have noticed that some transitions exhibit an asymmetric line profile (e.g., see Figs. 4 and C.1). Some of these asymmetry may be explained by the effect of Faraday rotation of the polarisation around frequencies of radical transitions. We were able to partially correct this effect by adding polarisation grids in front of the source and detector, as illustrated in Fig. D.1.

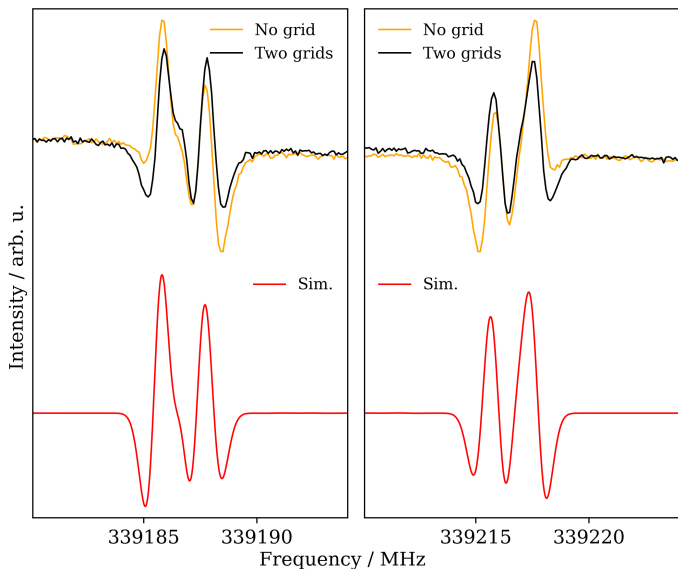


Fig. D.1. Experimental spectra of the $N'_{K'_a, K'_c} - N''_{K''_a, K''_c} = 16_{0,16} - 15_{0,15}$ transition of H₂NCO recorded without (in orange) and with (in black) polarisation grids, and comparison with a 300 K simulation obtained with PGOPHER using the final set of spectroscopic parameters (see Table 1) and a Gaussian profile with a full-width-at-half-maximum of 1 MHz.

For other transitions, the asymmetry of the transitions remained visible despite the use of the polarisation grids. This is striking for $K_a = 2$ transitions (the lowest and highest frequency components are systematically affected). To better understand this effect, we have recorded the $N'_{K'_a, K'_c} - N''_{K''_a, K''_c} = 15_{2,14} - 14_{2,13}$ a -type transition using conventional source-frequency-

modulation spectroscopy. The spectrum was acquired using a 48.157 kHz source frequency modulation (FM), a 360 kHz FM deviation, 100 kHz frequency steps, and an acquisition time of 150 ms per frequency point. The resulting spectrum is plotted on Fig. D.2 where it is compared with the spectrum recorded using Zeeman modulation. A portion of the spectrum on the FM trace is not exploitable because of saturation of the precursor transitions, a common caveat when investigating discharge products using source-frequency-modulation spectroscopy. Other weaker transitions arising from close-shell species are also visible (for instance around 320819 GHz). The acquisition using Zeeman-modulation strongly benefits from the open-shell species selectivity, as already mentioned in Chahbazian et al. (2024), although at the expense of the resolution since it yields broader features (the $K_a = 2$ transitions are particularly affected). By looking more closely at the two asymmetric components of the transition shown on Fig. D.2 (lower panels), we observe that the maximum of the positive component of the line does not correspond to the centre frequency of the transition. Special care was thus taken to retrieve experimental frequencies for these components, and a large frequency uncertainty (typically 300 kHz) was used in the fit.

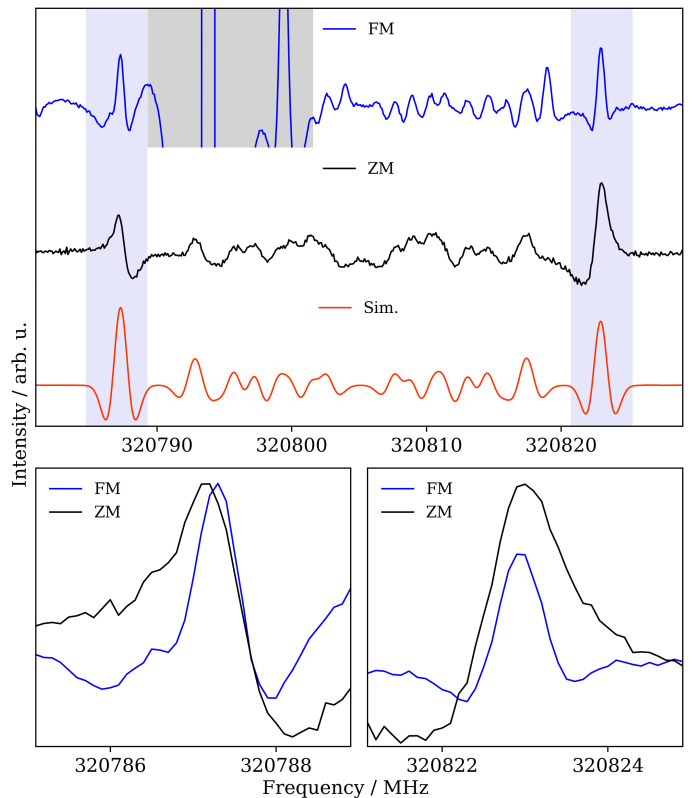


Fig. D.2. Experimental spectra recorded around the $N'_{K'_a, K'_c} - N''_{K''_a, K''_c} = 15_{2,14} - 14_{2,13}$ a -type transition of H₂NCO using source-frequency-modulation spectroscopy (FM) and Zeeman-modulation spectroscopy (ZM), and comparison with a 300 K simulation obtained with PGOPHER using the final set of spectroscopic parameters (see Table 1) and a Gaussian profile with a full-width-at-half-maximum of 1.5 MHz. The bottom panels show an overlap of the experimental spectra in the region highlighted in light blue on the top panel. The gray area on the upmost panel indicates a region where strong lines of the precursor prevent from observation of the radical product using the source-frequency-modulation experiment.

Presently, we do not fully understand the line profile observed in Zeeman-modulation, nor the asymmetry of some of the

components. It is interesting to note that the transitions particularly affected by the asymmetry already present some asymmetry in source-frequency-modulation spectroscopy, as visible in the lower panels of Fig. D.2, an effect that cannot be explained by the presence of unresolved hyperfine components. It is possible that these transitions are particularly affected by an external magnetic field (the Earth one in the case of the source-frequency-modulation spectrum). This would also be consistent with the fact that these transitions are overall stronger than other transitions on the Zeeman-modulation spectrum (as visible in Fig 4).

Appendix E: Vibrational satellites

The fundamental modes of H₂NCO calculated in this study are reported in Table A.1. At room temperature, the three lowest energy vibrational states $\nu_9 = 1$ (~ 282 cm⁻¹), $\nu_7 = 1$ (~ 540 cm⁻¹), and $\nu_8 = 1$ (~ 631 cm⁻¹) should possess significant population: 13 to 26% (based on the anharmonic and harmonic calculated energies), $\sim 7\%$, and $\sim 5\%$ of the ground state population, respectively. Indeed, on broad surveys of the experimental spectrum recorded using the Zeeman-modulation spectrometer (in particular in the 300–400 GHz range where we have a very good signal-to-noise ratio), we observe several clusters of similar shape of those of H₂NCO in $\nu = 0$, weaker and at lower frequencies. This is exemplified on Fig. E.1 where the most prominent clusters have been highlighted using three shading colours. The lines in the light purple regions exhibit an intensity of about 25% that of H₂NCO; they thus likely correspond to pure rotation in $\nu_9 = 1$. The clusters in the orange regions are about 10 times weaker than H₂NCO and thus may arise from transitions in $\nu_7 = 1$. Finally, a weak cluster is visible in the cyan region, with transitions intensities about 97% weaker than H₂NCO; they may correspond to either $\nu_8 = 1$ or $\nu_9 = 2$.

Unambiguous identification of vibrational satellites requires spectroscopic assignments in these excited vibrational states. Simulations of the pure rotational spectrum of H₂NCO in $\nu_9 = 1$, $\nu_7 = 1$, and $\nu_8 = 1$ are presented in the lower panel of Fig. E.1, alongside the final simulation in $\nu = 0$. The simulations have been obtained using the predicted rotational constants in the excited states (using the α values from our calculations, Table A.2); all the other parameters being kept fixed to those in $\nu = 0$. The harmonic energies of the excited states have been used since it was found to better reproduce the relative intensity of the transitions we believe are from $\nu_9 = 1$. The most convincing identification is perhaps $\nu_9 = 1$, with a prediction that appears only slightly shifted from the clusters observed in the experimental spectrum. Individual transition assignments, however, have proven challenging based on this portion of the spectrum only. Indeed, we have not performed systematic surveys over the entire spectral region, and even for the $N' - N'' = 17 - 16$ transition shown in the figure, the experimental measurements lack coverage in the regions where the $K_a = 0, 1$ and the lowest frequency $K_a = 2$ transitions lie. Dedicated measurements should be undertaken to fully unveil the spectrum of these vibrational satellites.

As a side note, Fig. E.1 also illustrates the somewhat anomalous intensities of the $K_a'' = 2$ a -type clusters on the experimental spectrum. These clusters indeed appear much stronger than what expected from the simulation, an effect that is visible over the entire submillimetre spectral region probed in this study. It is worth noting that these $K_a'' = 2$ clusters are also those that exhibit the most asymmetric line profile. It seems that they are the most sensitive to the modulation of the magnetic field (as mentioned already in section D).

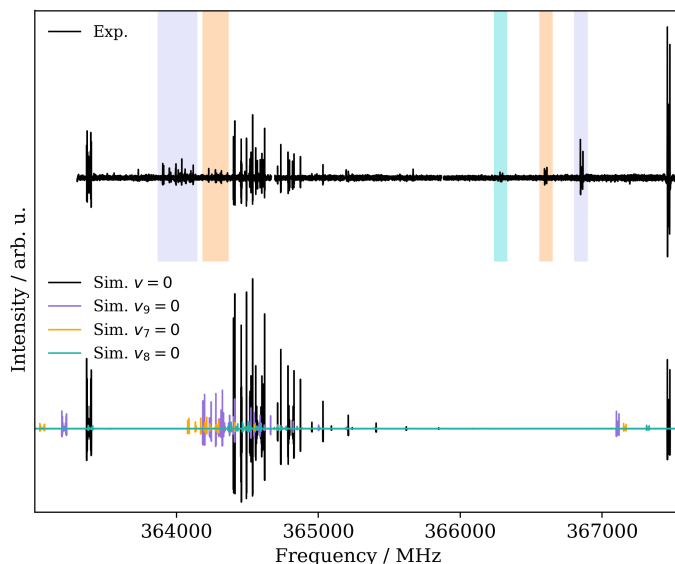


Fig. E.1. Experimental spectrum recorded around the $N' - N'' = 17 - 16$ a -type transition of H₂NCO (using Zeeman-modulation spectroscopy) (upper trace), and comparison with PGOPHER simulations for $\nu = 0$ and the three lowest vibrationally excited states at 300 K. The simulation in $\nu = 0$ has been obtained using the final set of spectroscopic parameters (see Table 1). Those in the excited states have been obtained using the harmonic vibrational energies, the predicted rotational constants in these states (calculated using the α values in Table A.2), and the other spectroscopic parameters from $\nu = 0$. For all simulations, a Gaussian profile with a full-width-at-half-maximum of 1.3 MHz has been used. Shaded areas in the upper trace highlight regions where the observed transitions likely arise from vibrational satellites.

Appendix F: Partition function

The rotational partition function has been calculated at various temperatures using SPCAT for the fully resolved hyperfine structure (since components are observed over the entire submillimetre-wave domain). Special care has been taken to ensure convergence of the partition function (which required calculation up to $J = 130$). Because the molecule possesses low-lying vibrational modes that are significantly populated at 300 K as seen in Appendix E, the vibration partition function has been calculated as well using the formula (Gordy & Cook 1984):

$$Q_{\text{vib}} = \prod_{i=1}^{N_{\text{vib}}} \frac{1}{1 - e^{-E_i(\text{vib})/kT}} \quad (\text{F.1})$$

where N_{vib} are the number of vibrational modes considered in the product, $E_i(\text{vib})$ is the vibrational energy of the i th vibrational mode (in cm⁻¹, see Table A.1), k is the Boltzmann constant (expressed in cm⁻¹/K for the sake of homogeneity), and T the temperature in Kelvin. Based on the results of the relative intensities of the $\nu_9 = 1$ vibrational satellites of H₂NCO observed on the experimental spectrum, that seem in agreement with the expected population assuming the harmonic energy if this mode, we decided to compute the harmonic value of the vibrational partition function ($Q_{\text{vib}} = Q_{\text{vib}}^{\text{harm}}$). For the calculation, we only considered the vibrational modes that holds significant population at room temperature, hence those with energies lower than 1000 cm⁻¹. Namely, these consist in $\nu_9 = 1$, $\nu_9 = 2$, $\nu_9 = 3$, $\nu_7 = 1$, $\nu_8 = 1$, $(\nu_9, \nu_7) = (1, 1)$, and $(\nu_9, \nu_8) = (1, 1)$. To total partition function is then obtained using the formula:

$$Q_{\text{tot}} = Q_{\text{rot}} Q_{\text{vib}} \quad (\text{F.2})$$

The different values are reported in Table F.1.

The catalogue intensities values reported in the electronic supporting information have been calculated using $Q_{\text{tot}}(300\text{ K})$. Intensities at lower temperatures can be recalculated using the corresponding $Q_{\text{tot}}(T)$ values.

Table F.1. Rotational, vibrational, and total partition functions for H_2NCO (fully resolved hyperfine structure) at various temperatures.

T / K	Q_{rot}	Q_{vib}	Q_{tot}
300.000	175482.9765	1.7259	302864.9020
225.000	113906.6451	1.3102	149235.8570
150.000	61973.9769	1.0860	67304.9490
75.000	21916.3156	1.0045	22016.0110
37.500	7761.8791	1.0000	7762.0343
18.750	2755.3989	1.0000	2755.3989
9.375	982.4627	1.0000	982.4627

Appendix G: $\text{FC}(\text{O})\text{NH}_2$

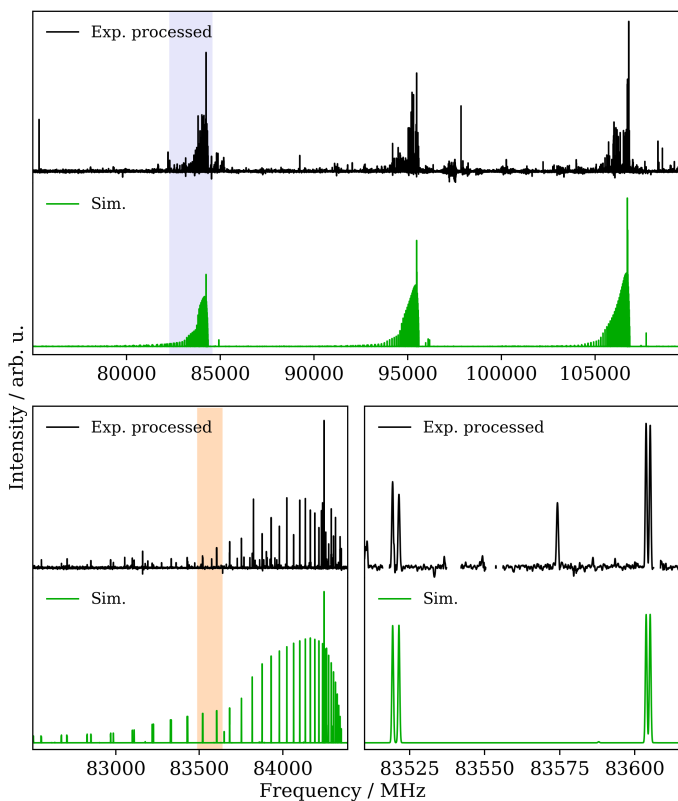


Fig. G.1. CP experimental spectrum after processing allowing to remove contributions from known close-shell species (upper trace), and comparison with a PGOPHER simulation for $\text{FC}(\text{O})\text{NH}_2$ in $\nu = 0$. The simulation has been obtained using the final set of spectroscopic parameters (see Table G.1), a temperature of 300 K, and a Gaussian profile with a full-width-at-half-maximum of 0.6 MHz. The shaded area in light purple in the upper panel is zoomed-in in the bottom left panel; that in orange is zoomed-in in the lower right panel. Discontinuities in the processed experimental spectrum correspond to region where lines of other molecules were lying.

Upon assignment of transitions from known molecules on the CP-FTMMW spectrum, we have observed three clusters of transitions, lying around 84, 95, and 106 GHz, as shown in Fig. G.1. These lines were rapidly assigned to $\text{FC}(\text{O})\text{NH}_2$ for

Table G.1. Spectroscopic parameters of $\text{FC}(\text{O})\text{NH}_2$ in the S -reduction and relevant fit information. 1σ error are reported within parentheses in the unit of the last digit; they have been formatted using the PIFORM software developed by Kisiel (2001).

Parameter	units	Lit. ^a	Exp. $\nu = 0$
A	/MHz	11304.39	11304.4357(40)
B	/MHz	11176.14	11176.1677(37)
C	/MHz	5616.06	5616.1001(32)
D_J	/kHz		5.078(29)
D_{JK}	/kHz		3.571(35)
D_K	/kHz		2.576(36)
d_1	/kHz		-3.1269(30)
d_2	/kHz		-0.9523(19)
H_{JK}	/Hz		0.312(14)
H_{KJ}	/Hz		-0.428(26)
H_K	/Hz		0.185(20)
h_2	/Hz		0.01144(58)
$3/2\chi_{aa}(\text{N})$	/MHz		3.63(14)
$1/4(\chi_{bb} - \chi_{cc})(\text{N})$	/MHz		1.484(34)
$\# / n^b$		96/46	1181 + 96/215 + 46
$J'_{\text{max}}, K'_{a\text{max}}$		7, 6	50, 42
RMS ^c	/MHz		0.102
σ^d			1.02

^a Rigden & Jackson (1966)

^b Number of lines (#) and number of different frequencies (n)

^c Root mean square value

^d Weighted standard deviation

which transitions in $\nu = 0$ have previously been measured in the 16–40 GHz range by Rigden & Jackson (1966) using Stark spectroscopy ($J' \leq 4, K'_a \leq 6, 46$ different frequencies). A fit of the literature transitions with a Watson-S Hamiltonian using the Pickett’s SPFIT software has enabled spectral predictions in the W-band range and assignments of the observed transitions of that molecules. We assigned 215 lines (both a - and b -type) corresponding to transitions involving $J' \leq 50$ and $K'_a \leq 42$. Many of the transitions exhibit a partially resolved nitrogen hyperfine structure. Because of unresolved asymmetric splitting for most of the transitions, the total number of lines in the fit is much larger (1277 total). Transitions from Rigden & Jackson (1966) and the CP-FTMMW spectrum were assigned a 100–200 kHz and 50–150 kHz frequency uncertainty, respectively. The resulting spectroscopic parameters are reported in Table G.1 and a simulation using these constants is shown in Fig. G.1. The corresponding fit files are available in the electronic supplementary material.

Appendix H: HNCHO

HNCHO was investigated by quantum-chemical calculations in a similar fashion as its H_2NCO isomer at the $\omega\text{B97X-D/cc-pVQZ}$ level of theory. The radical possesses two planar conformations, both belonging to the C_s point group of symmetry; namely *cis* (H-N-C-O dihedral angle of 0°) and *trans* (H-N-C-O dihedral angle of 180°), the latter lying 10.5 kJ/mol higher than the former. Both conformer are displayed in Fig. H.1 along with relevant structural information. The permanent dipole moment projections take values of $\mu_a = 0.7$ Debye and $\mu_b = 0.2$ Debye for the *cis* conformer and $\mu_a = 2.0$ Debye and $\mu_b = 2.7$ Debye for the *trans* one. The predicted spectroscopic constants for these two conformers are reported in Table H.1.

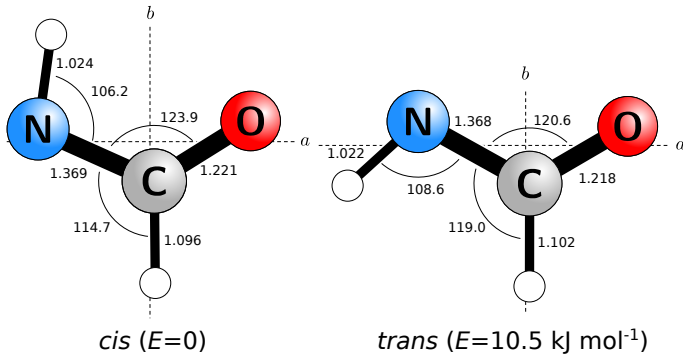


Fig. H.1. Equilibrium structure of *cis* and *trans* HNCHO calculated at the ω B97X-D/cc-pVQZ level of theory. Geometrical parameters (bond lengths in angstroms and angles in degrees) and principal axes of inertia are reported. The figure was generated using the PMIFST software from the PROSPE collection of programs developed by Kisiel (2001).

Table H.1. Calculated spectroscopic parameters (in MHz) of HNCHO *cis* and *trans* conformers in the *S*-reduction.

Parameter	<i>cis</i>	<i>trans</i>
<i>A</i>	72610.71	81883.12
<i>B</i>	12407.62	12028.24
<i>C</i>	10596.84	10487.66
D_N	0.01003	0.007903
D_{NK}	0.02089	0.09529
D_K	1.256	1.962
d_1	-0.002003	-0.001256
d_2	-0.000264	-0.000230
ϵ_{aa}	-2388.	-2170.
ϵ_{bb}	-109.4	-100.1
ϵ_{cc}	3.848	3.910
$a_F(\text{N})$	14.23	13.21
$3/2T_{aa}(\text{N})$	-52.84	-51.24
$1/4(T_{bb} - T_{cc})(\text{N})$	-26.17	-26.12
$T_{ab}(\text{N})$	-0.3635	0.1979
$3/2\chi_{aa}(\text{N})$	-6.366	0.4001
$1/4(\chi_{bb} - \chi_{cc})(\text{N})$	-1.523	-2.569
$\chi_{ab}(\text{N})$	-2.542	0.7746
$a_F(\text{H}_1)$	4.403	5.531
$3/2T_{aa}(\text{H}_1)$	7.770	7.732
$1/4(T_{bb} - T_{cc})(\text{H}_1)$	2.032	2.017
$T_{ab}(\text{H}_1)$	-5.602	-4.618
$a_F(\text{H}_2)$	-50.29	-51.25
$3/2T_{aa}(\text{H}_2)$	-60.65	15.19
$1/4(T_{bb} - T_{cc})(\text{H}_2)$	13.90	0.2089
$T_{ab}(\text{H}_2)$	9.995	47.63

^a The calculated *A*, *B*, *C* rotational constants have been Bayesian corrected by a 0.9866 factor (see Lee & McCarthy 2020), all the other calculated parameters are equilibrium values.